



Article

Study on the Flow Behavior of 5052 Aluminum Alloy over a Wide Strain-Rate Range with a Constitutive Model Based on the Arrhenius Model Extension

Huijuan Ma^{1,2,3} , Peiliao Wang^{1,2,3}, Xiang Huang^{1,2,3}, Wenjie Mao^{1,2,3}, Zhiang Gong^{1,2,3}, Mao Zhang⁴  and Hui Zhu^{5,*}

- ¹ Hubei Key Laboratory of Advanced Technology for Automotive Components, Wuhan University of Technology, Wuhan 430070, China; mahuijuan21@whut.edu.cn (H.M.); 258247@whut.edu.cn (P.W.); hx0032@whut.edu.cn (X.H.); maowenjie@whut.edu.cn (W.M.); gong-zhiang@whut.edu.cn (Z.G.)
² Hubei Collaborative Innovation Center for Automotive Components Technology, Wuhan 430070, China
³ Hubei Research Center for New Energy & Intelligent Connected Vehicle, Wuhan 430070, China
⁴ State Key Laboratory of Materials Processing and Die & Mould Technology, School of Materials Science and Engineering, Huazhong University of Science and Technology, Wuhan 430074, China; zhangmao@hust.edu.cn
⁵ Department of Mechanical Engineering, The University of Sheffield, Sheffield S1 3JD, UK
* Correspondence: hui.zhu@sheffield.ac.uk

Abstract: The formability at room temperature and low speed limits the application of aluminum alloy, while high strain rates positively improve the formability of materials. The constitutive behaviors of materials under high strain rates or impact loadings are significantly different from those under quasi-static conditions, while few constitutive models consider the effect of the mobile dislocation and forest dislocation evolution on the dynamic strain aging (DSA) over a wide strain-rate range. The 5052 aluminum alloy, of which the primary source of strain-hardening is dislocation–dislocation interaction, is widely used in manufacturing automotive covering parts and is considered one of the most promising alloys. Therefore, this study conducts uniaxial tensile tests on AA5052-O under conditions of temperatures ranging from 293 K to 473 K and strain rates ranging from 0.001 s^{-1} to 3000 s^{-1} , and compares the stress–strain relationships of AA5052-O under different conditions to illustrate the constitutive relationship affected by the dislocation evolution over a wide strain-rate range. The Arrhenius model based on the thermal activation mechanism is modified and extended by considering the effects of dynamic strain aging (DSA), drag stress, and the evolution of mobile dislocation and forest dislocation. Thus, a new physics-based constitutive model for AA5052-O is proposed, which can well reflect the change in strain-rate sensitivity with the strain rate increasing. The mobile dislocation density and total dislocation density are predicted with a modified Kubin–Estrin (KE) model, and the influences of variable mobile dislocation on DSA and dislocation drag are discussed as well. In order to verify the reliability of the new constitutive model, the dislocation densities of the specimens before and after deformation are obtained with TEM and XRD, which are in good agreement with the predicted values. This study also compares the newly proposed model with classic constitutive models using multiple statistical evaluation methods, which shows that the new physics-based constitutive model has not only more clear physical meanings for its parameters but also has a higher prediction accuracy.

Keywords: constitutive model; high strain rate; dynamic strain aging; microstructure; dislocation evolution; Arrhenius model



Citation: Ma, H.; Wang, P.; Huang, X.; Mao, W.; Gong, Z.; Zhang, M.; Zhu, H. Study on the Flow Behavior of 5052 Aluminum Alloy over a Wide Strain-Rate Range with a Constitutive Model Based on the Arrhenius Model Extension. *Metals* **2023**, *13*, 1948. <https://doi.org/10.3390/met13121948>

Academic Editor: Frank Czerwinski

Received: 31 October 2023

Revised: 19 November 2023

Accepted: 21 November 2023

Published: 28 November 2023



Copyright: © 2023 by the authors. Licensee MDPI, Basel, Switzerland. This article is an open access article distributed under the terms and conditions of the Creative Commons Attribution (CC BY) license (<https://creativecommons.org/licenses/by/4.0/>).

1. Introduction

The formability of aluminum sheets limits their application in complex-shaped products, such as automotive body parts. And scholars have proven that high-strain-rate forming techniques such as electromagnetic forming (EMF), explosive forming (EF), and electro-hydraulic forming (EHF) may improve the formability of sheet metal [1–4], and these

techniques also have the advantages of simple die design, high workpiece accuracy, good surface quality, and especially strong plastic deformation ability, making high-strain-rate forming an ideal processing technology for materials with lower formability [5]. Thomas et al. [6] proposed that the forming limit of 6063-T6 aluminum alloy under electromagnetic tube bulging is 2–3 times higher than that under quasi-static forming. Balanethiram and Daehn [7] believed that the improvement in formability is due to the change in the material constitutive relationship under high strain rates.

The studies mentioned above indicate that the strain rate has a significant effect on the deformation mechanism of aluminum alloys. It is necessary to conduct in-depth research and establish suitable constitutive models to achieve well-controlled forming processes and produce high-quality components. AA5052 has been widely used in the manufacturing of automotive and aircraft sheet metal parts and critical components due to its excellent high strength-to-weight ratio, corrosion resistance, and weldability [8–10]. And the main source of strain-hardening of AA5052 is the dislocation–dislocation interaction, so AA5052-O is studied in this paper to illustrate the constitutive relationship related to the dislocation evolution over a wide strain-rate range.

Constitutive models are widely used for analyzing deformation behavior and predicting flow stress and are of great significance for optimizing process parameters. Chen et al. [11] adopted the normalized dislocation density to evaluate the strain hardening and proposed a dislocation mechanics-based plane stress material model, which could be used for designing process windows, taking into account the formed shape as well as the post-formed properties. Santos et al. [12] developed an elastic-viscoplastic constitutive formulation for polycrystalline FCC metals subjected to high-strain-rate cold deformation and discussed thermal activation and dislocation drag mechanisms. Fan et al. [13] studied the influence of deformation temperature on the flow stress of the 2A12 aluminum alloy, and found that after subtracting the structural component, related to grain size, dislocations, and precipitates, from the total flow stress, a bell-shaped flow stress was left in some specific temperature regions, which can be explained well with the dynamic strain aging mechanism. Because the typical dislocation density-based K-M model could not capture the negative strain-rate sensitivity caused by DSA, Dong et al. [14] proposed a modified K-M model considering DSA to describe the tensile behavior of alloys, while relevant tests were conducted at low strain rates and the reliability of the model in the wide strain-rate range has not been verified.

Wang et al. [15] used the Arrhenius model to establish a strain compensation constitutive model for AA5052 in the temperature range of 573–723 K. In fact, the Arrhenius model has been widely used in the study of the thermal forming of materials [16–20] and can reflect the mechanical properties of materials at different temperatures and low strain rates well. However, there has been almost no research applying the Arrhenius model to deformation under high-strain-rate conditions thus far, which is partly because the Arrhenius model is based on the thermal activation mechanism and does not consider the influence of dynamic strain aging under different strain rates and drag stress at high strain rates.

To better illustrate the constitutive relationship affected by multiple mechanisms over a wide strain-rate range of aluminum alloy, this paper establishes a physically-based constitutive model for AA5052-O based on experimental results under conditions of temperature ranging from 293 K to 473 K and strain rates ranging from 0.001 to 3000 s^{−1} to study the constitutive behavior of AA5052-O over a wide range of strain rates. The effects of the mobile dislocation and forest dislocation evolution on the thermal activation mechanism, dynamic strain aging, and dislocation drag mechanism are discussed, and the dislocation evolution is depicted by a modified Kubin–Estrin model. The result shows that the new constitutive model can well reflect the change in the strain-rate sensitivity with the strain rate increases and the prediction accuracy is higher than that of existing models.

2. Materials and Experiments

2.1. Materials

The applied material was the AA5052-O alloy from Chinalco Southwest Aluminum Co., Ltd., (Chongqing, China) and the mechanical properties of AA5052-O are listed in Table 1. The heat treatment state was fully annealed, and the original grain size was 40–80 μm . The chemical composition of AA5052-O from the optical emission spectroscopy is given in Table 2.

Table 1. Mechanical properties of AA5052-O [21].

Item	Tensile Strength (MPa)	Yield Strength (Mpa)	Elongation after Fracture (%)
Standard	170–215	≥ 65	≥ 14

Table 2. Chemical composition of AA5052-O (in wt%).

Element	Mg	Si	Fe	Cu	Mn	Zn	Cr	Al
Standard	2.2–2.8	≤ 0.25	≤ 0.40	≤ 0.10	≤ 0.10	≤ 0.10	0.15–0.35	Remainder
Actual	2.40	0.055	0.26	0.02	0.05	0.02	0.15	Bal.

2.2. Experiments

2.2.1. Uniaxial Tensile Tests

The geometry of low-strain-rate and dynamic tensile specimens are shown in Figure 1a,b, respectively. All the specimens for a low strain rate are machined from an aluminum alloy plate with the thickness of 1 mm. The procedures of low-strain-rate experiments are documented in detail in ISO 6892-1:2019 [22], and the process of dynamic experiments is in line with Khan [23].

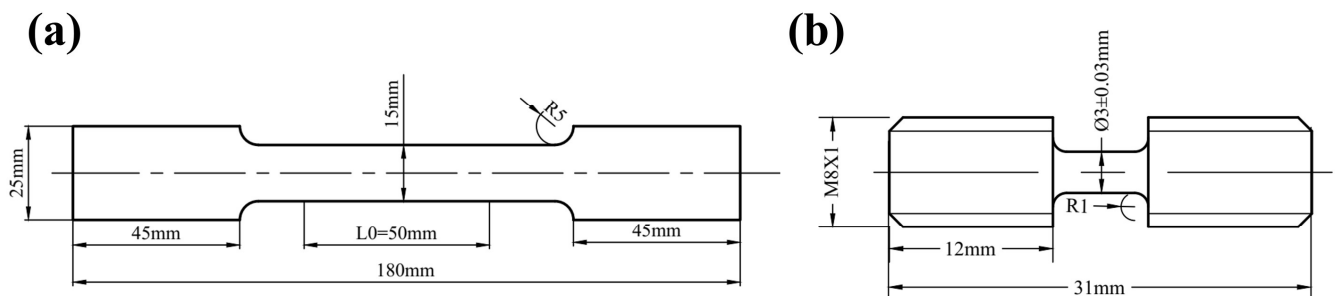


Figure 1. Schematic of (a) low-strain-rate tensile specimens (ISO 6892) and (b) dynamic tensile specimens.

The low-strain-rate tensile tests were conducted under different temperatures ($T = 293, 373, 473 \text{ K}$), at a quasi-static ($\dot{\epsilon} = 0.001 \text{ s}^{-1}$) strain rate, and under different strain rates ($\dot{\epsilon} = 0.001, 0.01, 0.1 \text{ s}^{-1}$) at room temperature ($T = 293 \text{ K}$), using an AG-100KN material mechanical properties testing machine from Shimadzu (Kyoto, Japan) and a Gleeble3500 thermal simulation testing machine from Data Sciences International, Inc. (Wilmington, DE, USA), as shown in Figure 2a,b. The specimens were kept at the desired temperature for 30 min before starting the test to obtain a uniform temperature. At least three experiments were conducted for each quasi-static condition to ensure the reliability of the experimental results. The engineering stress σ_e and engineering strain ϵ_e were calculated from Equations (1) and (2).

$$\sigma_e = \frac{f}{A_s} \quad (1)$$

$$\epsilon_e = \frac{d}{l} \quad (2)$$

where A_s , l , f , and d are the cross-sectional area of the specimen, the gauge length of the specimen, the measured load, and the displacement data measured by an extensometer, respectively.

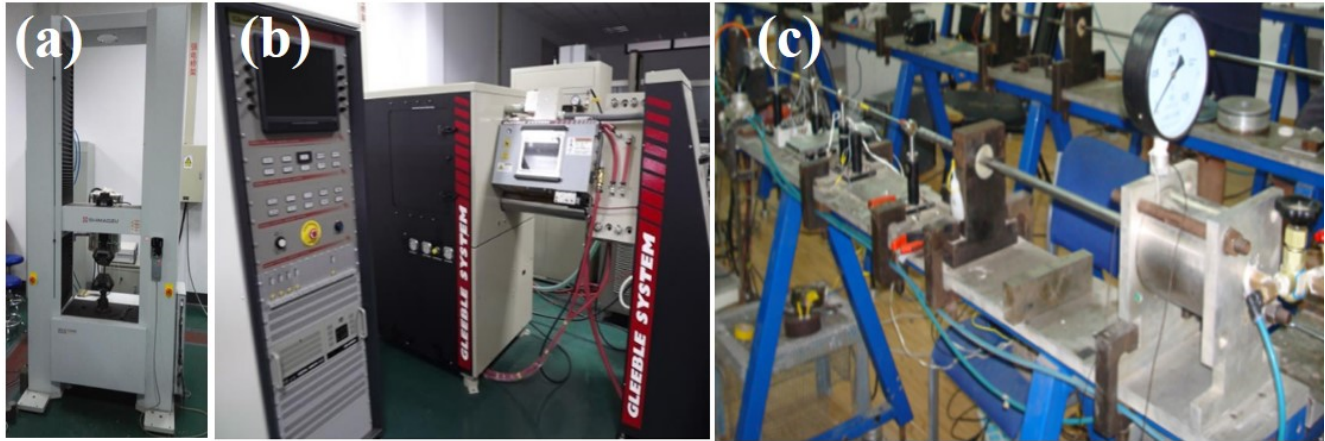


Figure 2. The test equipment (a) the AG-100KN material mechanical properties testing machine, (b) the Gleeble3500 thermal simulation testing machine, (c) the split Hopkinson tension bar device.

The dynamic tensile tests were performed with a split Hopkinson tension bar device as shown in Figure 2c. The stress–strain results were measured at strain rates of $\dot{\epsilon} = 1000, 2000, 3000 \text{ s}^{-1}$ under room temperature ($T = 293 \text{ K}$). The experimental devices include a high-pressure gas gun, a sleeve striker, an incident bar with an end cap, a transmission bar, and a measuring signal acquisition device, as shown in Figure 3.

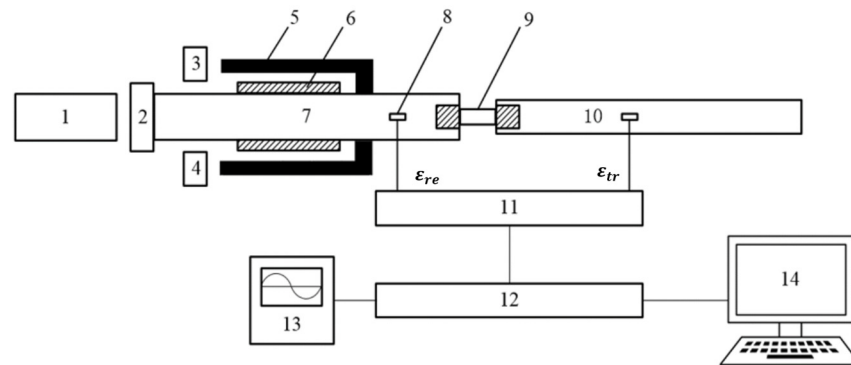


Figure 3. The schematic diagram of the split Hopkinson tension bar equipment: 1—momentum trap; 2—end cap; 3—laser generator; 4—laser receiver; 5—gas gun; 6—sleeve striker; 7—electric resistance strain gauge; 8—incident bar; 9—tensile specimen; 10—transmission bar; 11—super dynamic strain gauge; 12—transient waveform storage; 13—oscilloscope; 14—computer.

The engineering stress σ_e and engineering strain ϵ_e in the sample can be calculated from the reflected and transmitted strain wave signals collected by the strain gauge [24].

$$\sigma_e(t) = \frac{A_b E}{A_s} \epsilon_{tr}(t) \quad (3)$$

$$\dot{\epsilon}(t) = -\frac{2C_b}{l_s} \epsilon_{re}(t) \quad (4)$$

$$\epsilon_e(t) = \int_0^t \dot{\epsilon}(t) dt \quad (5)$$

where A_b is the cross-sectional area of the bar, l_s is the length of the specimen; ε_{re} and ε_{tr} are the signals of the incident rod and transmission rod, respectively; E and C_b are, respectively, the elastic modulus and elastic wave velocity of the rod.

Based on the assumption of volume invariance, the true stress σ_t and the true strain ε_t of the specimen were calculated from the engineering stress σ_e and engineering strain ε_e .

$$\sigma_t = \sigma_e(1 + \varepsilon_e) \quad (6)$$

$$\varepsilon_t = \ln(1 + \varepsilon_e) \quad (7)$$

2.2.2. Microscopic Testing

The dislocation distribution morphologies of the fracture specimens were observed by a JEM-2100 transmission electron microscope (TEM) (JEOL, Tokyo, Japan). Specimens for TEM observation were punched into 3 mm-diameter disks from slices, and mechanically thinned down to a 40–60 μm thickness. Then, the disks were thinned on the Struers TenuPol-5 electrolytic double spray instrument (Struers, Ballerup, Denmark), and the sample meeting the requirements of TEM observation was prepared.

The X-ray diffraction (XRD) data of the samples were obtained by Rigaku SmartLab SE type X-ray diffractometer (Rigaku, Tokyo, Japan). The scanning speed of the X-ray diffractometer was $2^\circ/\text{min}$, and the scanning range was $10\sim 90^\circ$.

3. Results

3.1. Stress–Strain Curves

The main focus of this work is to study the deformation process of AA5052-O under different strain rates and different temperatures. Non-uniform deformation occurs during the tensile process of the specimen, which affects the calculation of the true stress, and necking is the starting point of non-uniform deformation and strain localization during tension. The occurrence of necking in this study is determined based on the modified Considère criterion proposed by Weber [25]. Figures 4 and 5 show the flow stress–plastic strain curves of the specimen under different strain rates and temperatures. The solid line represents the uniform deformation zone, the dashed line represents the non-uniform deformation zone, and the starting point of necking occurs at the junction of the two.

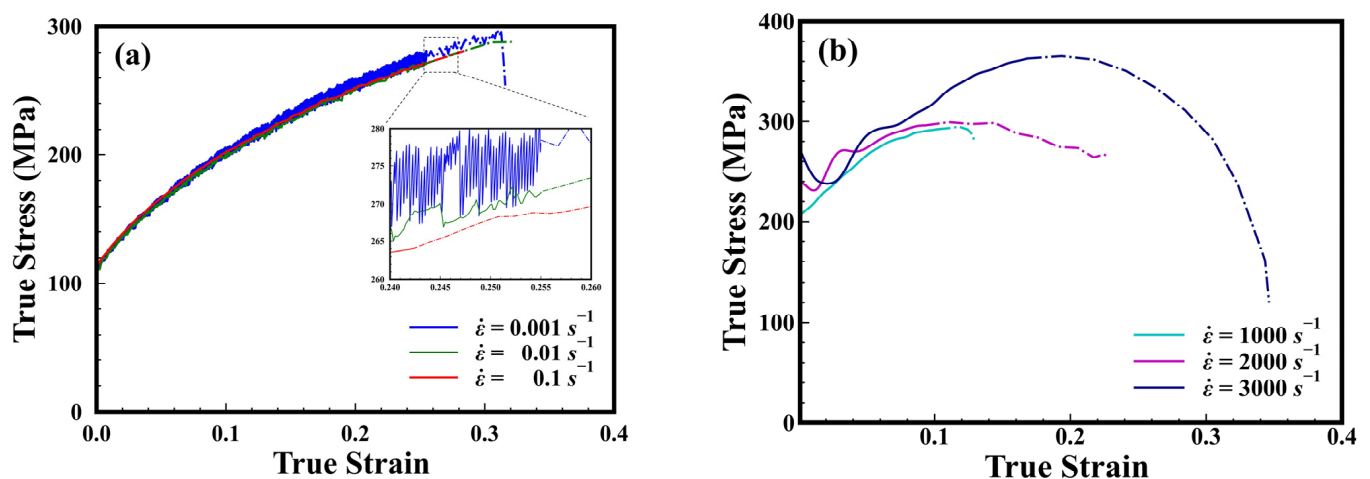


Figure 4. Stress–strain relationship of AA5052-O at different strain rates ($T = 293 \text{ K}$): under (a) low strain rates; (b) high strain rates.

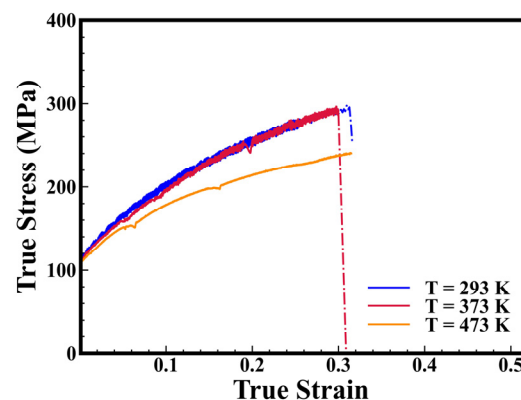


Figure 5. Stress–strain relationship of AA5052-O at different temperatures ($\dot{\epsilon} = 0.001 \text{ s}^{-1}$).

The strain-rate sensitivity exponent (m) indicates the sensitivity of flow stress to the strain rate during the plastic deformation of a material. A larger strain-rate sensitivity exponent m represents the better ability of the material to deform uniformly, resulting in better formability. And the value of m can be obtained by Equation (8) [26]:

$$m = \left. \frac{\partial \ln \sigma}{\partial \ln \dot{\epsilon}} \right|_{\epsilon, T} \quad (8)$$

As shown in Figure 4a, under low-strain-rate conditions, AA5052-O exhibits a low strain-rate sensitivity (SRS), the flow stress obtained at a strain rate of 0.01 s^{-1} is close to or even slightly lower than that at a strain rate of 0.001 s^{-1} , and m varies from -0.008 to 0.007 according to Equation (8). The Portevin–Le Chatelier (PLC) effect of a serrated pattern is also observed. Both the low or negative strain-rate sensitivity and PLC effect suggest the existence of dynamic strain aging (DSA) in AA5052-O. Under the high-strain-rate conditions in Figure 4b, obvious positive SRS appears, and the maximum value of m can reach 0.7 . With increasing strain rate, the necking and fracture of the material occur later. Comparing the tensile results of the material under low-strain-rate and high-strain-rate conditions, it can be observed that necking occurs earlier in the high strain rate deformation samples. Under the conditions of 1000 s^{-1} and 2000 s^{-1} , the material fracture occurs earlier compared to the low-strain-rate conditions. However, as the strain rate reaches 3000 s^{-1} , the elongation of the material significantly increases and is higher than the maximum elongation obtained under low-strain-rate conditions, indicating that high-speed forming can improve the formability limit of the material. Figure 5 shows the effect of different temperatures on the flow stress under quasi-static conditions. No obvious temperature softening phenomenon is observed when the temperature increases from 293 K to 373 K . However, with a further increase in temperature to 473 K , the flow stress drops sharply, which may be due to the acceleration of dislocation generation and annihilation mechanisms at higher deformation temperatures. At low strain rates, the dislocations and rearrangements caused by thermal deformation have enough time to be canceled out, resulting in a lower flow stress.

3.2. TEM Analysis

Figure 6 shows the dislocation morphology of AA5052-O specimens after quasi-static and high-strain-rate tensile deformation. It can be seen that the dislocation density is low and the dislocation cells are large under the quasi-static condition in Figure 6a, and a higher dislocation density and smaller dislocation cells are observed under the high-strain-rate condition in Figure 6c. At high strain rates, the atomic diffusion rate is accelerated and the grain boundary diffusion and migration ability are enhanced, so multiple dislocation slip systems are activated and dislocations from different slip systems cross each other, thus forming many dislocation cell structures, which can improve the plasticity of the material [27]. Therefore, a high strain rate leads to a high dislocation density, resulting in a

smaller size of the dislocation cell structure. The combination of dislocation entanglement and smaller dislocation cells can lead to a lower dislocation moving speed, which increases the flow stress of the material. In addition, the parallel dislocation walls loaded on a particular plane are also observed under the high strain rate in Figure 6d, which are typical dislocation arrangement features of planar slip mode and can be attributed to the short range order (SRO) of an Al-Mg solid solution. The destruction of SRO after continuous activations of dislocations under planar stress reduces the local resistance to dislocation movement, thus limiting the movement of the dislocation in a few planes, which is conducive to plane slip [28,29]. And the generation of long parallel dislocation walls in Figure 6d indicates a higher planar stress to realize continuous activations of dislocations in a short time.

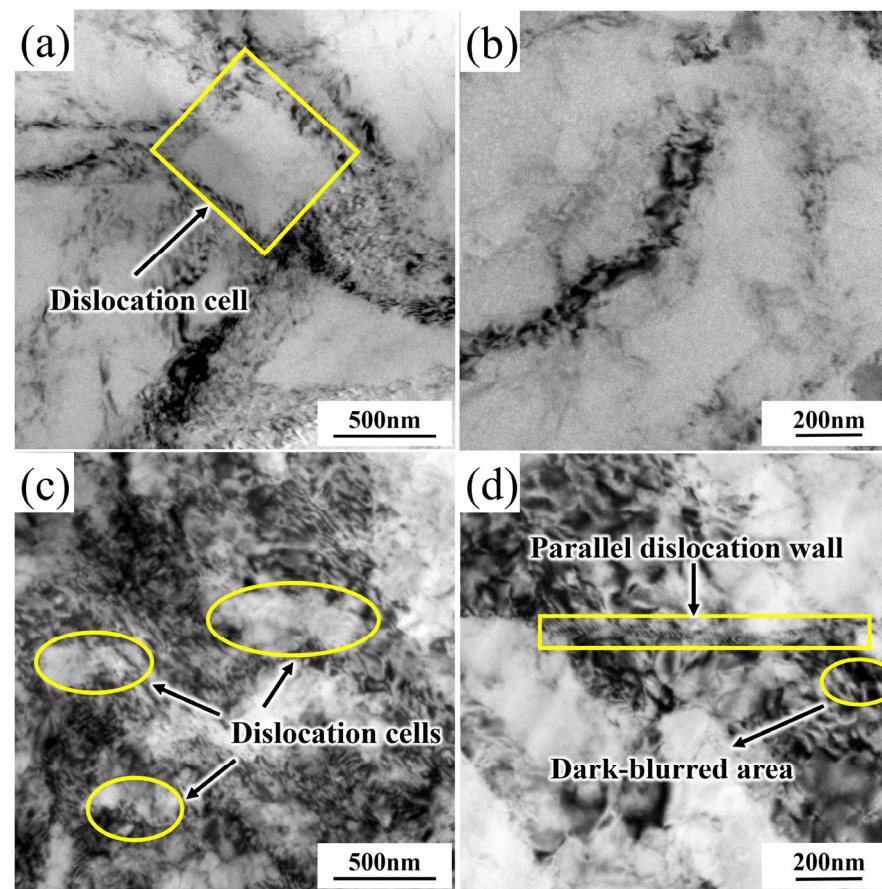


Figure 6. TEM micrographs showing the dislocation configurations of specimens at different strain rates: (a,b) quasi-static tensile test ($\dot{\epsilon} = 0.001 \text{ s}^{-1}$, $\epsilon_p = 0.315$); (c,d) SHTB test ($\dot{\epsilon} = 3000 \text{ s}^{-1}$, $\epsilon_p = 0.348$).

The residual dislocation density can be estimated by statistical analysis of TEM images to perform quantitative analysis on the microstructural evolution of materials. Each TEM image of a grain substructure can be divided into three regions: (i) areas without visible dislocations, (ii) areas with visible dislocation lines, and (iii) dark and blurry areas [30]. For areas with visible dislocation lines, a method is employed whereby a grid consisting of multiple horizontal and vertical lines is overlaid on the area to be measured [31]. When dislocation lines strongly overlap, they appear as dark, blurry regions (tightly intertwined) in TEM, where individual lines cannot be distinguished. The above method cannot calculate a reliable dislocation density for such entangled dislocations. To address this issue, it can be assumed that dislocation lines are cylindrical lines with a diameter of d , corresponding to the minimum distance allowed by lattice distortion between neighboring lines. The geometric model of highly dense dislocations, which simulates the arrangement of blurry regions, is simplified as a prismatic bundle filled with cylindrical dislocations tightly

packed together. It should be emphasized that this model is a simplified representation of a possible arrangement, and the actual entanglement is a more complex arrangement. Based on this model, the total number of dislocations in the prismatic bundle is calculated to be:

$$\rho = \frac{1}{d^2} \quad (9)$$

According to Equation (9), the value of dislocation density in highly dense dislocation arrangements can be estimated by the inverse square of the measurement line diameter of a single dislocation. The value of d can be determined by individually visible dislocations close to the dark-blurred region. It is noteworthy that the dislocation density calculated by this method is the upper limit of the possible range of values [30]. Therefore, in this paper, the dislocation density near the dark-blurred region is used to replace the dislocation density in the dark-blurred region, obtaining the lower limit of the dislocation density. The final evaluation of the dislocation density is obtained by taking the median of the upper and lower limits.

Finally, the dislocation density of the entire TEM image is calculated based on the ratio of the area fraction of different regions.

$$\rho = A_1\rho_1 + A_2\rho_2 \quad (10)$$

A_1 and A_2 , respectively, refer to the percentage of the total area occupied by visible line areas and dark-blurred areas, while ρ_1 and ρ_2 refer to the dislocation density of the visible line areas and dark-blurred areas, respectively.

Finally, according to Equation (10), a statistical analysis was performed on the TEM images, and the results showed that under the quasi-static deformation condition ($\dot{\epsilon} = 0.001 \text{ s}^{-1}$, $\epsilon_p = 0.315$), the dislocation density of the sample was $1.5 \times 10^{14} \text{ m}^{-2}$, while under the high-speed deformation condition ($\dot{\epsilon} = 3000 \text{ s}^{-1}$, $\epsilon_p = 0.348$), the dislocation density was $8.77 \times 10^{14} \text{ m}^{-2}$.

3.3. X-ray Diffraction Analysis

Figure 7 shows a typical XRD spectrum of AA5052-O. No diffraction peaks were observed except the aluminum matrix in the diffraction pattern. From the partial enlarged detail of the (200) crystal plane, it can be seen that the full width at half maximum (FWHM) values of the stretched samples are significantly larger than those of the parent material. Under high-speed rate conditions, the FWHM of the sample is larger than that of the quasi-static condition. The increase in FWHM indicates the presence of a large number of lattice defects in the crystal, and the magnitude of this value can reflect the dislocation density of the material. As discussed earlier, it is difficult to calculate the dislocation density directly from TEM images when the dislocation density reaches a certain level. The appearance of tightly intertwined dislocations will exacerbate the difficulty in evaluating the dislocation density, bringing many difficulties and controversies to the quantitative characterization of dislocation strengthening [32]. Therefore, it is necessary to use the peak width of diffraction to estimate the approximate range of dislocation density. The modified Williamson–Hall equation was used to estimate the dislocation density ρ of deformed samples under different test conditions, as shown below [33]:

$$\frac{\beta \cdot \cos \theta}{k \cdot \lambda} = \frac{1}{D} + 2 \cdot \frac{\sin \theta}{k \cdot \lambda} \quad (11)$$

$$\rho = \frac{B \cdot \epsilon^2}{b^2} \quad (12)$$

where β is the full width at half maximum, D is the average particle size, λ is the wavelength of Cu K α radiation (\AA), θ is the diffraction angle, ϵ is the microstrain, k is a constant between 0.9 and 1, and b is the magnitude of the Burgers vector for Al (0.286 nm).

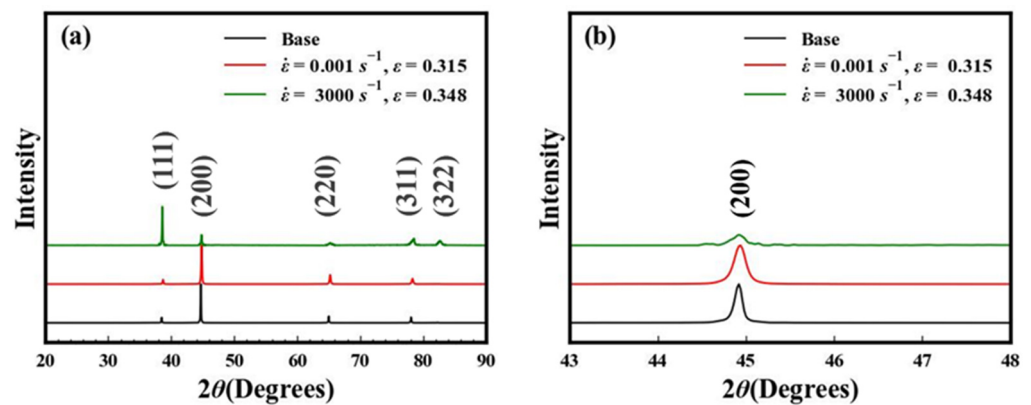


Figure 7. XRD patterns of specimens after uniaxial tensile tests at strain rates of 0.001 s^{-1} and 3000 s^{-1} : (a) full scanning range; (b) partial enlarged detail of the (200) crystal plane.

Research by Suo [34] and Lee [35] has shown that the dislocation density in the aluminum alloy in its undeformed state is $2.5 \times 10^{12} \text{ m}^{-2}$, while under quasi-static deformation conditions, the dislocation density is approximately 10^{14} m^{-2} . Based on the above formula, the dislocation densities before and after the deformation of the specimen under $\dot{\epsilon} = 0.001$ and 3000 s^{-1} conditions were calculated to be 1.59×10^{12} , 1.54×10^{14} , and $8.69 \times 10^{14} \text{ m}^{-2}$, respectively, which are close to the results of Suo and Lee. Additionally, the XRD calculations and TEM statistics are also in good agreement with the results.

4. Constitutive Model and Discussions

4.1. Development of the New Physically-Based Model with Extension of the Arrhenius Model

In this study, the flow stress is divided into the yield stress which can be predicted using a modified Arrhenius model, and the strain-related terms considering the effects of strain on the microstructure and stress, which avoids the difficulty in solving the changing parameters of a modified Arrhenius-type model in the process of deformation. Generally, dislocation strengthening is the main source of strain hardening, but the effects of strain on the DSA-related stress and the drag stress should also be considered:

$$\sigma = \sigma_y + \Delta\sigma_{\text{dis}} + \Delta\sigma_{\text{D}} + \Delta\sigma_{\text{drag}} \quad (13)$$

where σ_y is the yield stress, $\Delta\sigma_{\text{dis}}$, $\Delta\sigma_{\text{D}}$, and $\Delta\sigma_{\text{drag}}$, respectively, represent the stress increments related to the dislocation strengthening mechanism induced by strain, DSA-related stress variation, and the attenuation of drag stress.

4.1.1. Yield Stress Component

The Arrhenius formula is the most successful formula for explaining the relationship between strain-rate constants and temperature [36]. Studies have shown that the main factors affecting the high-temperature tensile flow stress of metallic materials are the strain rate, deformation temperature, and strain. Based on the Arrhenius formula, Sellars and Tegart proposed that the relationship between flow stress, temperature, and strain rate under high-temperature plastic deformation conditions can be represented by a hyperbolic sine formula containing the deformation activation energy Q and temperature T [37]:

$$\dot{\epsilon} = A [\sinh(\alpha_A \sigma_y)]^{n_A} \cdot \exp\left(-\frac{Q}{RT}\right) \quad (14)$$

where $\dot{\epsilon}$ is the strain rate, R is the molar gas constant ($8.314 \text{ J}/(\text{mol} \cdot \text{K})$), σ_y is the yield stress (MPa), A is a temperature-independent constant, n_A is the stress exponent, which reflects the relationship between strain rate and stress, and α_A is a material constant. This model is also known as the Arrhenius constitutive model, which can well describe the

relationship between stress, temperature, and strain rate and is the most widely used model for predicting the flow behavior of materials at high temperatures [16].

From the results of the stress–strain relationship, it is known that AA5052-O exhibits prominent characteristics of dynamic strain aging, while the Arrhenius-type model is mainly based on the thermal activation mechanism. Therefore, it can be anticipated that it cannot characterize the constitutive relationship of AA5052-O. In this paper, the stress component related to the dynamic strain aging mechanism is separated, and the Arrhenius-type model is preliminarily modified:

$$\dot{\varepsilon} = A [\sinh(\alpha_A (\sigma_y - \sigma_D))]^{n_A} \cdot \exp\left(-\frac{Q}{RT}\right) \quad (15)$$

where σ_D represents the stress component related to the dynamic strain aging mechanism, which will be further discussed in subsequent chapters.

Currently, the application of the Arrhenius constitutive model is mainly focused on the analysis of the constitutive relationship of materials under high-temperature conditions and low strain rates. However, as the strain rate continues to increase, the effect of the drag stress caused by phonon action on the flow stress gradually strengthens. Therefore, the preliminary modified Arrhenius constitutive model still has obvious limitations. Based on the relationship between the macroscopic strain rate and dislocation motion established by the Hungarian metallurgical engineer Orowan [38] (as Equation (16)), this study further modified the model for predicting the flow stress of aluminum alloys at larger strain rates.

$$\dot{\varepsilon} = M b \rho_m \bar{v} \quad (16)$$

In the equation, $\dot{\varepsilon}$ represents the macroscopic strain rate, M is the Taylor factor, b is the Burgers vector, ρ_m is the mobile dislocation density, and \bar{v} represents the average dislocation velocity, which can be given by Equation (17) [39]:

$$\bar{v} = \frac{l}{t_w + t_l} \quad (17)$$

where l is the free path, i.e., the distance between two short-range obstacles. The total time required for a mobile dislocation to complete a single free path includes the waiting time for thermal activation at the obstacle (t_w) and the sliding time during the free path (t_l). When the strain rate is low, the waiting time of the mobile dislocation at the obstacle is much greater than the sliding time t_l . The preliminary modified Arrhenius constitutive model can be used to reflect the thermal activation process. When the effect of dislocation drag is considered, i.e., the sliding time of dislocation during the free path cannot be ignored, then:

$$v_l = \frac{1}{t_l} = \frac{b \left(\frac{\sigma_y}{M} - \bar{\tau} \right)}{B} \quad (18)$$

where v_l is the dislocation sliding velocity, b is the Burgers vector, B is the viscosity coefficient related to the material and temperature, and $\bar{\tau}$ represents the long-range stress [26], which can be calculated by the equation:

$$\bar{\tau} = \alpha G b \sqrt{\rho} + \tau_0 \quad (19)$$

Among them, $\alpha G b \sqrt{\rho}$ represents the long-range obstacle caused by dislocation density, τ_0 represents the initial defect of the material; α is the Taylor constant and ρ is the total dislocation density. The modified Arrhenius constitutive equation can be obtained from Equations (17)–(19):

$$\dot{\varepsilon} = \frac{b \rho_m}{\frac{B}{b \left(\frac{\sigma_y}{M} - \bar{\tau} \right)} + \frac{b \rho_m}{A [\sinh(\alpha_A (\sigma_y - \sigma_D))]^{n_A} \exp\left(-\frac{Q}{RT}\right)}} \quad (20)$$

where the Taylor factor M , the size of the Burgers vector b , the viscosity coefficient B , and the molar gas constant R are common material constants that can be obtained directly from the reference literature [40,41].

4.1.2. Dislocation Strengthening Component of Flow Stress

One of the most surprising findings in plasticity theory is the relationship between stress and the dislocation density ρ caused by dislocation strengthening. If the influence of dislocation density on stress in the yield stress is not ignored, the increase in flow stress related to the dislocation density can be expressed as follows:

$$\Delta\sigma_{\text{dis}} = \alpha G M b (\sqrt{\rho} - \sqrt{\rho_y}) \quad (21)$$

where ρ_y is the total dislocation density when yielding occurs.

4.1.3. DSA Component of Flow Stress

In numerous experimental studies, a significant additional hardening caused by the dynamic strain aging phenomenon has been reported. Without considering the effect of dynamic strain aging, it is not possible to accurately predict the behavior of materials. Based on the model proposed by McCormick, Jiang et al. [42] characterized the stress component caused by DSA:

$$\sigma_D = \gamma C^* \quad (22)$$

γ represents the pinning strength of a solute atom per unit dislocation movement, C^* represents the concentration of solute atoms in the mobile dislocation line, and the value of C^* during deformation is determined by the effective aging time t_a . During the effective aging time t_a , solute atoms diffuse to temporarily obstructed dislocations and can be expressed by the modified saturation Cottrell–Bilby strain-aging kinetics [43].

$$C^* = C_s^* [1 - \exp(-\beta t_a^{n_D})] \quad (23)$$

In the equation, C_s^* represents the saturation value of the solute atom concentration, β is a material parameter for the diffusivity of solute atoms, t_a is the effective pinning time of solute atoms to moving dislocations, and n_D is a material parameter related to the diffusion characteristic exponent. The gap between t_a and t_w is ignored, and the effect of DSA is significant only at low strain rates, where $t_l \ll t_w$, so t_a is approximately equal to:

$$t_a \approx \frac{M \rho_m b l}{\dot{\epsilon}} \quad (24)$$

where l is the free slip distance that the dislocation migrates during the deformation process, which is almost the same as the spacing distance d between adjacent dislocations. Considering the distribution of dislocations, the quantitative relationship between l and ρ can be described by Equation (25) [40]:

$$l = 1/\sqrt{\rho} \quad (25)$$

Because heat can provide energy for the movement of point defects, the temperature can affect the motion of solute atoms and vacancies. At low temperatures and high strain rates, the diffusion rate of solute atoms is lower than the corresponding dislocation velocity, resulting in a weak dynamic strain-aging effect. At high temperatures and low strain rates, solute atoms move with dislocations, and their diffusion rate is higher than the corresponding dislocation velocity, resulting in solute atom clusters that do not pin the

dislocations and weaken the effect of DSA. Therefore, the final expression for considering the temperature effect on DSA is:

$$\sigma_D = D_s [1 - \exp(-\beta \left(\frac{M \rho_m b}{\dot{\epsilon} \sqrt{\rho}} \right)^{n_D})] \exp\left[-\left(\frac{T - T_{SA}}{\xi}\right)^2\right] \quad (26)$$

where $D_s = \gamma C_s^*$, representing the saturation strength of solute atoms, T_{SA} is the temperature corresponding to the peak stress of DSA, where the interaction between dislocations and solute atoms is the strongest, and ξ reflects the temperature range of DSA [44].

4.1.4. Drag Stress Attenuation

Moreover, during deformation, the mobile dislocations in the material rapidly multiply, causing a decrease in the velocity and drag stress. Therefore, when considering the effect of plastic strain on flow stress, the drag stress attenuation term should be considered:

$$\Delta \sigma_{\text{drag}} = \frac{M B \dot{\epsilon}}{b^2 \rho_{my}} \times \left(\frac{\rho_{my}}{\rho_m} - 1 \right) \quad (27)$$

4.1.5. Evolution of Internal State Variables

The mechanical response of materials is closely associated with the density of the mobile dislocations and the total dislocations, and the new physically-based model takes the mobile dislocation density and the total dislocation density as internal state variables. Therefore, exploring the evolution law of dislocation density with strain is necessary. Due to the short duration of dynamic deformation and the fact that the deformation temperature rise is insufficient to reach the recrystallization temperature within the range of deformation parameters studied in this paper, it is believed that there is no dynamic recrystallization and grain growth phenomenon, mainly considering the proliferation of dislocations and dynamic recovery. Kubin and Estrin proposed that the evolution of the forest dislocation density ρ_f and the mobile dislocation density ρ_m were related to the multiplication, mutual annihilation and capture of mobile dislocations, fixed effect due to interactions of mobile dislocations with forest dislocations, and dynamic recovery of forest dislocations [45]. The research of Csanádi [46] shows that the reduction in the density of mobile dislocations during the plastic deformation of fcc metals can essentially be attributed to capture mechanisms related to the mutual annihilation and capture, and both the formation and the annihilation of forest dislocations are controlled by non-conservative motion activated by dislocation thermal energy. According to the hypothesis of Csanádi, both the densities of forest dislocation and mobile dislocation are 0.5 times the initial total dislocation density ρ_0 , and the KE model can be simplified to:

$$\rho_m = \frac{C_1}{C_2} - \frac{C_1 - C_2 \rho_{m0}}{C_2} \exp(-C_2 \epsilon_p) \quad (28)$$

$$\rho = \frac{2C_1}{C_2} - \left(\frac{2C_1}{C_2} - \rho_0 \right) \left(1 + \frac{C_2 \epsilon_p}{2} \right) \exp(-C_2 \epsilon_p) \quad (29)$$

where C_1 is a parameter related to the multiplication of mobile dislocations, and C_2 is associated with the capture of mobile dislocations and the annihilation of forest dislocations.

Previous studies have shown that deformation behavior is significantly influenced by the deformation temperature and strain rate, while deformation parameters determine the evolution of the dislocation density. Therefore, the parameters C_1 and C_2 can be modified as functions of the temperature and strain rate:

$$C_1 = A_1 \left(\dot{\epsilon} \exp\left(\frac{Q_{c1}}{RT}\right) \right)^{n_{c1}} \quad (30)$$

$$C_2 = A_2 \left(\dot{\epsilon} \exp\left(\frac{Q_{c2}}{RT}\right) \right)^{n_{c2}} \quad (31)$$

where A_1 , Q_{c1} , n_{c1} , A_2 , Q_{c2} , and n_{c2} are all material constants.

Using Equations (19)–(31), a new constitutive model based on the Arrhenius model is obtained. In this model, the yield stress is obtained from the modified Arrhenius constitutive equation, which decouples the DSA effect with the thermal activation process and considers the sliding process of dislocation during the free path. The decoupling of the DSA component can effectively avoid the difficulty in predicting yield stress due to the competition between the effects of DSA and the thermal activation mechanism, and provide a more powerful prediction ability compared with the monotonous original Arrhenius equation. And the consideration of the sliding process of dislocation helps to explain the sharp increase in the stress due to the viscosity at high strain rates. The strengthening effect caused by strain is reflected by the dislocation strengthening component $\Delta\sigma_{dis}$, the DSA-related stress variation $\Delta\sigma_D$, and the attenuation of drag stress $\Delta\sigma_{drag}$, which are all strongly associated with the dislocation density. Thus, the KE model is modified as a submodel to derive the internal variable of dislocation density. The complete form of the model is shown below, where ρ_{ym} , ρ_y , and σ_{yD} represent the density of mobile dislocations, total dislocation density, and DSA stress component at yield ($\epsilon_p = 0$), respectively. The newly proposed model is based on the Arrhenius model and takes into account the effects of DSA, dislocation strengthening, and stress drag. And if the material does not have the DSA effect, the relevant term can be deleted.

$$\left\{ \begin{array}{l} \sigma = \sigma_y + \Delta\sigma_{dis} + \Delta\sigma_D + \Delta\sigma_{drag} \\ \dot{\epsilon} = \frac{\sigma_y + \Delta\sigma_{dis} + \Delta\sigma_D + \Delta\sigma_{drag}}{b\rho_{ym}} \frac{b\rho_{ym}}{b\left(\frac{\sigma_y}{M} - \bar{\tau}\right) + A\left[\sinh\left(\alpha_A(\sigma_y - \sigma_{yD})\right)\right]^{n_A} \exp\left(-\frac{Q}{RT}\right)} \\ \sigma_{yD} = D_s \left[1 - \exp\left(-\beta \left(\frac{M\rho_{ym}b}{\dot{\epsilon}\sqrt{\rho_y}}\right)^{n_D}\right) \exp\left[-\left(\frac{T-T_{SA}}{\xi}\right)^2\right] \right] \\ \bar{\tau} = \alpha G b \sqrt{\rho_y} + \tau_0 \\ \Delta\sigma_{dis} = \alpha G M b \left(\sqrt{\rho} - \sqrt{\rho_y}\right) \\ \Delta\sigma_D = D_s \left[\left(-\beta \left(\frac{M\rho_{ym}b}{\dot{\epsilon}\sqrt{\rho_y}}\right)^{n_D}\right) - \exp\left(-\beta \left(\frac{M\rho_{ym}b}{\dot{\epsilon}\sqrt{\rho}}\right)^{n_D}\right) \exp\left[-\left(\frac{T-T_{SA}}{\xi}\right)^2\right] \right] \\ \Delta\sigma_{drag} = \frac{MB\dot{\epsilon}}{b^2\rho_{my}} \times \left(\frac{\rho_{my}}{\rho_m} - 1\right) \\ \rho_m = \frac{C_1}{C_2} - \frac{C_1 - C_2\rho_0/2}{C_2} \exp(-C_2\epsilon_p) \\ \rho = \frac{2C_1}{C_2} - \left(\frac{2C_1}{C_2} - \rho_0\right) \left(1 + \frac{C_2(\epsilon_p + \epsilon_{comp})}{2}\right) \exp(-C_2\epsilon_p) \\ C_1 = A_1 \left(\dot{\epsilon} \exp\left(\frac{Q_{c1}}{RT}\right)\right)^{n_{c1}} \\ C_2 = A_2 \left(\dot{\epsilon} \exp\left(\frac{Q_{c2}}{RT}\right)\right)^{n_{c2}} \end{array} \right. \quad (32)$$

4.2. Establishment of the New Constitutive Model

The new model was established for AA5052-O based on experimental data. Some of the parameters were directly obtained from the reference literature, while the remaining model parameters must be determined with an optimization algorithm. The genetic algorithms model the process of natural selection as an optimization protocol and are a well-established class of evolutionary methods suitable for solving minimization or maximization problems, even when the search space is large and the topology is complex, which means it is suitable for multi-parameter optimization in our study. However, the maintenance of a large population pool and the staged modeling of fitness-dependent selection, reproduction, and mutation processes require a large number of merit function (fitness) assessments per iteration, and are therefore computationally costly [47]. Thus, the gradient-based Levenberg–Marquardt algorithm, which costs less computation per iteration and is more efficient, was coupled into the iteration to accelerate convergence. Figure 8 is the flowchart illustrating the hybrid optimization method.

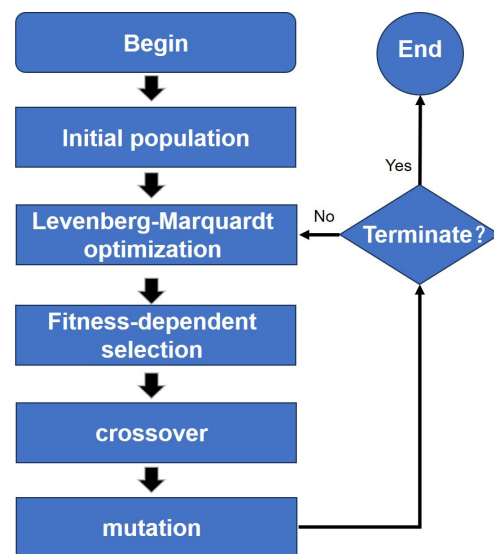


Figure 8. The flowchart illustrating the hybrid optimization method.

The fitness function used in the optimization process is as shown in Equation (33).

$$\text{fit} = \frac{1}{\sum_{i=1}^{n_i} \sum_{j=1}^{n_j} \sum_{k=1}^{n_k} \left(\frac{\sigma_{\text{pre}}^{\text{ijk}} - \sigma_{\text{exp}}^{\text{ijk}}}{\sigma_{\text{exp}}^{\text{ijk}}} \right)^2} \quad (33)$$

where $\sigma_{\text{pre}}^{\text{ijk}}$ and $\sigma_{\text{exp}}^{\text{ijk}}$ are the predicted stress and experimental stress at a strain of ε_{p_i} , a strain rate of $\dot{\varepsilon}_j$, and a temperature of T_k , respectively.

The crossover probability is set as 0.6, the mutation probability is set as 0.2, and the termination condition is the number of iterations reaching 400. The final model parameters are shown in Table 3.

Table 3. Material parameters and constants for AA5052-O.

Parameter	Value	Reference
α	0.5	Huang [40]
M	3.06	Huang [40]
b	$2.86 \times 10^{-10} \text{ m}$	Zaretsky [41]
B/T	$7.5 \times 10^{-8} \text{ Pa} \cdot \text{s} \cdot \text{K}^{-1}$	Zaretsky [41]
R	$8.314 \text{ J/mol} \cdot \text{K}$	Nieto-Fuentes [48]
G	26,654 Pa	Adjusted
ρ_0	$1.59 \times 10^{12} \text{ m}^{-2}$	Experiment
τ_0	32.88 MPa	Adjusted
A	3.127×10^5	Adjusted
A_1	$1.010 \times 10^{15} \text{ m}^{-2}$	Adjusted
A_2	16.335	Adjusted
Q	13.85 kJ/mol	Adjusted
Q_{c1}	14.53 kJ/mol	Adjusted
Q_{c2}	132.788 kJ/mol	Adjusted
α_A	5.932×10^{-3}	Adjusted
n_A	15.654	Adjusted
n_{c1}	0.088	Adjusted
n_D	1.078	Adjusted
γC_s^*	102.3 MPa	Adjusted
β_1	2.159×10^{-9}	Adjusted
T_{SA}	346.788 K	Adjusted
ξ	186.396 K	Adjusted

Figures 9 and 10 are comparison charts between the predicted results of the new model and the experimental results. As shown in Figure 9, the model can well reflect the stress–strain relationship under different strain rates at room temperature. Figure 9a shows that the model predicted the negative strain-rate sensitivity of AA5052-O at low strain rates. The yield stress at a strain rate of $\dot{\epsilon} = 0.001 \text{ s}^{-1}$ was close to that at a strain rate of $\dot{\epsilon} = 0.01 \text{ s}^{-1}$, but the flow stress at a strain rate of $\dot{\epsilon} = 0.001 \text{ s}^{-1}$ was higher than that at a strain rate of 0.01 s^{-1} when the strain increased to a certain value. At high strain rates, the predicted values of the model shown in Figure 9b are also close to the experimental results, especially when $\dot{\epsilon} = 3000 \text{ s}^{-1}$, where the predicted values and experimental results are basically on the same curve. As shown in Figure 10, the predicted results of the model for the stress–strain relationship under different temperature conditions at quasi-static conditions are also relatively ideal: when the temperature rises from 273 K to 373 K, the predicted flow stress shows no significant changes, but when the temperature rises from 373 K to 473 K, the predicted flow stress decreases significantly, which is highly consistent with the experimental results. In Section 5 of this paper, the model accuracy was evaluated with indicators such as the correlation coefficient, mean absolute relative error, and root mean square error.

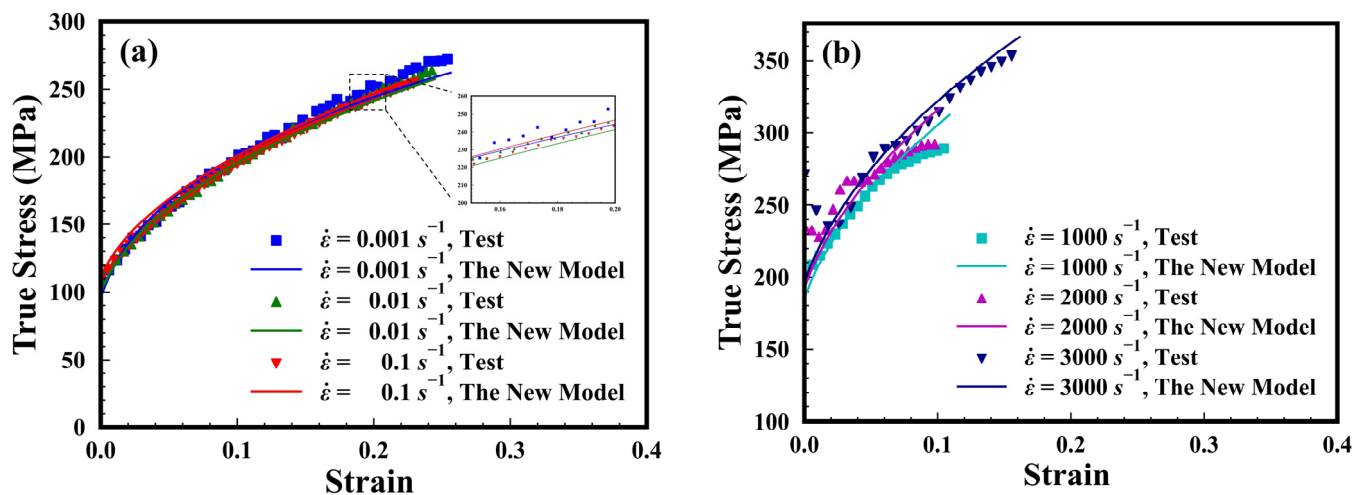


Figure 9. Comparison between the experimental results and the new model predicted stress–strain relations under (a) low strain rates ($T = 293 \text{ K}$); (b) high strain rates ($T = 293 \text{ K}$).

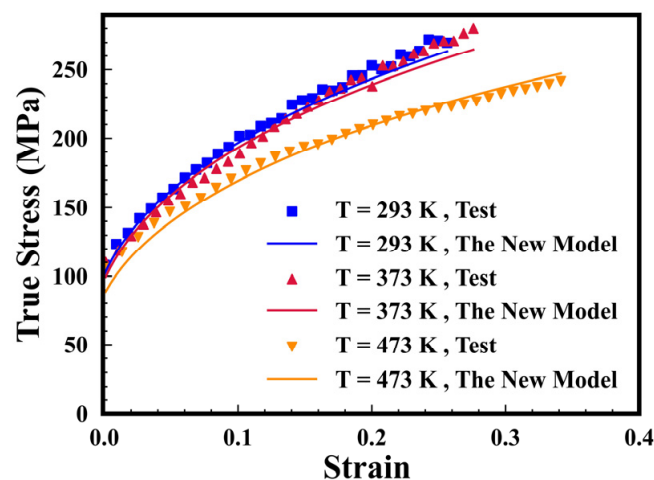


Figure 10. Comparison between the experimental results and the new model predicted stress–strain relations under different temperatures ($\dot{\epsilon} = 0.001 \text{ s}^{-1}$).

4.2.1. Prediction of Yield Stress by the New Constitutive Model

Figure 11 compares the predicted yield stress of AA5052-O of the new constitutive model based on a modified Arrhenius model and the traditional Arrhenius-type model. The modified model shows that the yield stress exhibits strain-rate insensitivity within the range of $0.001\text{--}1\text{ s}^{-1}$, which can be attributed to the competition between dynamic strain aging and thermal activation mechanisms. As the strain rate increases, the stress component caused by dynamic strain aging decreases, offsetting some of the stress increment caused by the thermal activation mechanism, hence exhibiting strain-rate insensitivity. However, as the strain rate further increases, the influence of dynamic strain aging on yield stress decreases to a negligible level, and the thermal activation mechanism dominates, which can explain that the yield stress significantly increases with the strain rate within the range of $1\text{ to }10^4\text{ s}^{-1}$. When the strain rate reaches 10^5 s^{-1} , dislocation drag becomes the dominant stress-influencing mechanism, and the yield stress sharply increases. In contrast, the traditional Arrhenius-type model only considers the effect of thermal activation, and the predicted results do not accord with the experimental values.

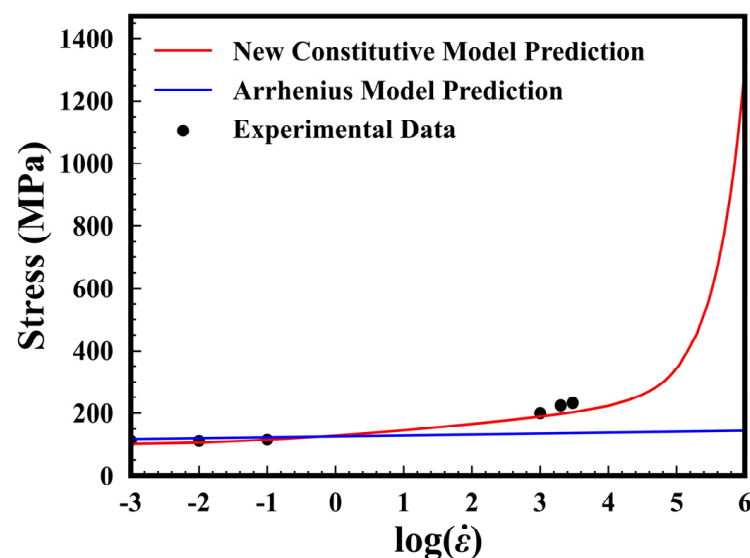


Figure 11. Prediction of the yield stress of AA5052-O by a modified Arrhenius-type model and traditional Arrhenius-type model.

4.2.2. Prediction of Dislocation Density by the New Constitutive Model

The constitutive model constructed in this study uses the mobile dislocation density and the total dislocation density as internal state variables, so the prediction of dislocation density is critical to the entire work. Figure 12 shows the relationship between the dislocation density and strain predicted by the newly established constitutive model under different strain rates. The initial dislocation density, calculated from XRD experimental data, is $1.59 \times 10^{12}\text{ m}^{-2}$. As shown in Figure 12, within the range of strain in the sample experiment, the proliferation and recovery of dislocations did not reach dynamic equilibrium, which is consistent with the results of the stress–strain curve obtained from experiments. Table 4 compares the model prediction results of dislocation density, TEM statistical results, and XRD data calculation results, and the maximum relative error is less than 26% at the strain rate of 0.001 s^{-1} and less than 14.2% at the strain rate of 3000 s^{-1} , indicating that the KE model modified by temperature and strain rate has a good predictive performance for dislocation density. It also proves that the newly established constitutive model is reliable to some extent.

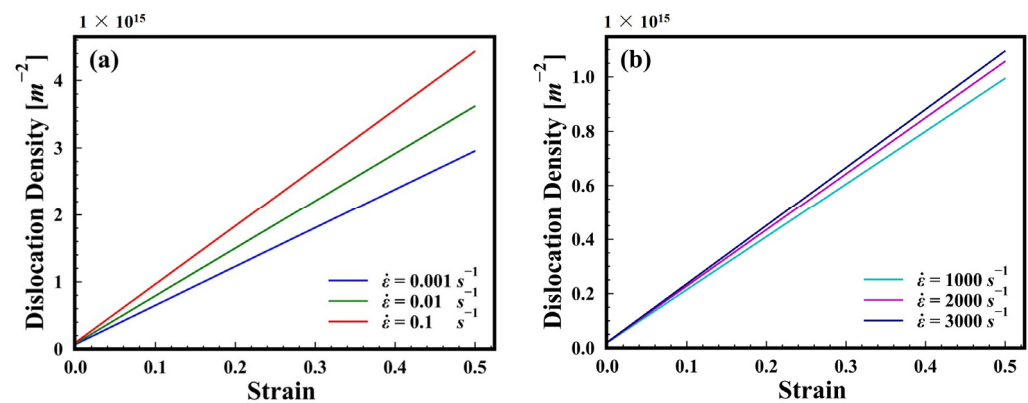


Figure 12. Predicted relationship between the dislocation density and strain under (a) low strain rates ($T = 293$ K); (b) high strain rates ($T = 293$ K).

Table 4. The dislocation densities from model prediction result, TEM statistical results, and XRD data calculation results.

	$\dot{\epsilon} = 0.001 \text{ s}^{-1}$, $\epsilon_p = 0.315$	$\dot{\epsilon} = 3000 \text{ s}^{-1}$, $\epsilon_p = 0.348$
TEM result	$1.5 \times 10^{14} \text{ m}^{-2}$	$8.77 \times 10^{14} \text{ m}^{-2}$
XRD result	$1.54 \times 10^{14} \text{ m}^{-2}$	$8.69 \times 10^{14} \text{ m}^{-2}$
Prediction	$1.89 \times 10^{14} \text{ m}^{-2}$	$7.68 \times 10^{14} \text{ m}^{-2}$

4.3. Evaluation of the New Constitutive Model

Several statistical evaluation methods were adopted to scientifically evaluate the predictability of the newly proposed constitutive model for AA5052-O over a wide strain-rate range and compare the new model with classic constitutive models such as the modified Johnson–Cook (J-C) model [49], the modified Cowper–Symonds (C-S) model [5], the modified Field–Backofen (F-B) model [50], and the modified Zerilli–Armstrong (Z-A) model [51]. These methods include the correlation coefficient (R_{CC}), mean absolute relative error (AARE), and root mean square error (RMSE), which can be expressed as:

$$R_{CC} = \frac{\sum_i^N (E_i - \bar{E})(P_i - \bar{P})}{\sqrt{\sum_i^N (E_i - \bar{E})^2 (P_i - \bar{P})^2}} \quad (34)$$

$$AARE = \frac{1}{N} \sum_i^N \left| \frac{E_i - P_i}{E_i} \right| \quad (35)$$

$$RMSE = \sqrt{\frac{1}{N} \sum_i^N (E_i - P_i)^2} \quad (36)$$

where E_i represents the experimental value and P_i represents the predicted value. \bar{E} and \bar{P} are the averages of E_i and P_i , respectively. N represents the total number of data used in this study.

The correlation coefficient R_{CC} is a commonly used statistical parameter that provides information about the strength of the linear relationship between experimental values and predicted values. However, a higher R_{CC} value does not necessarily mean a better prediction performance, as the model may tend towards higher or lower values [52]. Therefore, this study also used AARE and RMSE as evaluation indicators. These two indicators are unbiased statistical measures of the predictability of the model or equation, as they are calculated by comparing the relative errors on a per-item basis.

Table 5 presents the results of different evaluation metrics for each model, where the correlation coefficient R_{CC} for all models is higher than 0.9, indicating a good correlation between the results obtained by each model and the experimental data. However, as R_{CC} values are not directly related to the prediction performance [52], the focus is on comparing the magnitudes of the AARE and RMSE values for each model. It can be seen that the newly established new model has the smallest relative error with respect to the experimental results, with the smallest AARE and RMSE values, indicating that this new model has certain advantages over traditional models. In addition, the modified C–S and J–C models have AARE and RMSE values that are closer to ideal values compared to the modified F–B and Z–A models, suggesting a better fitting result.

Table 5. Correlation coefficient (R_{CC}), mean absolute relative error (AARE), and root mean square error (RMSE) of constitutive models.

Type of Model	R_{CC}	AARE	RMSE
The new model	0.990	0.028	10.004
Modified J–C model	0.999	0.033	13.712
Modified C–S model	0.999	0.048	11.870
Modified F–B model	0.994	0.063	17.133
Modified Z–A model	0.999	0.069	15.555

Figure 13 shows a comparison between experimental and predicted values of different models at different strain rates. The results indicate that under low-strain-rate conditions, the stress predictions based on the modified F–B model and the modified Z–A model do not match the experimental results and cannot accurately describe the constitutive behavior of AA5052-O during high-strain-rate forming processes. In particular, at strain rates of 0.001 s^{-1} and 0.1 s^{-1} , the predicted values deviate significantly from the experimental values, which may be due to the existence of DSA mechanisms, making it difficult for the modified F–B and Z–A models to make reasonable predictions of the flow stress of AA5052-O in the low-strain-rate range. With the accumulation of strain, the densities of mobile dislocation and forest dislocation increase rapidly, resulting in dislocation strengthening. At the same time, the increasing mobile dislocation density will lead to the longer effective time of dynamic strain aging, which will also cause strengthening. Although the dislocation density tends to multiply more rapidly at high strain rates, which means a higher dislocation strengthening, the strengthening induced by DSA is a nonlinear response. Therefore, the combined effect of the two strengthening effects eventually leads to similar flow stresses at different strain rates in the low-strain-rate range, which is difficult to be expressed by traditional models, especially when fitting the data obtained at a wide strain-rate range. However, in the high-strain-rate region, the predictions of these models are closer to the experimental data, which can be attributed to the gradual reduction in the DSA effects with increasing strain rate. The modified J–C model shows a good predictive performance in the low-strain-rate region and is very close to the predicted results of the new model, but in the high-strain-rate region, especially at a strain rate of 3000 s^{-1} , the predicted values of the modified J–C model are too large. Although the modified C–S model coupled with the strain and strain rate shows a larger deviation from the experimental values in the low-strain-rate region compared to the new model and the modified J–C model, it can still describe the flow behavior well overall, even though this model fails to provide an explanation for the changes in the constitutive relationship with strain and strain rate from a mechanical point of view. In contrast, the newly established constitutive model can predict the flow stress well at all strain rates and provides an explanation from a microscopic mechanism perspective.

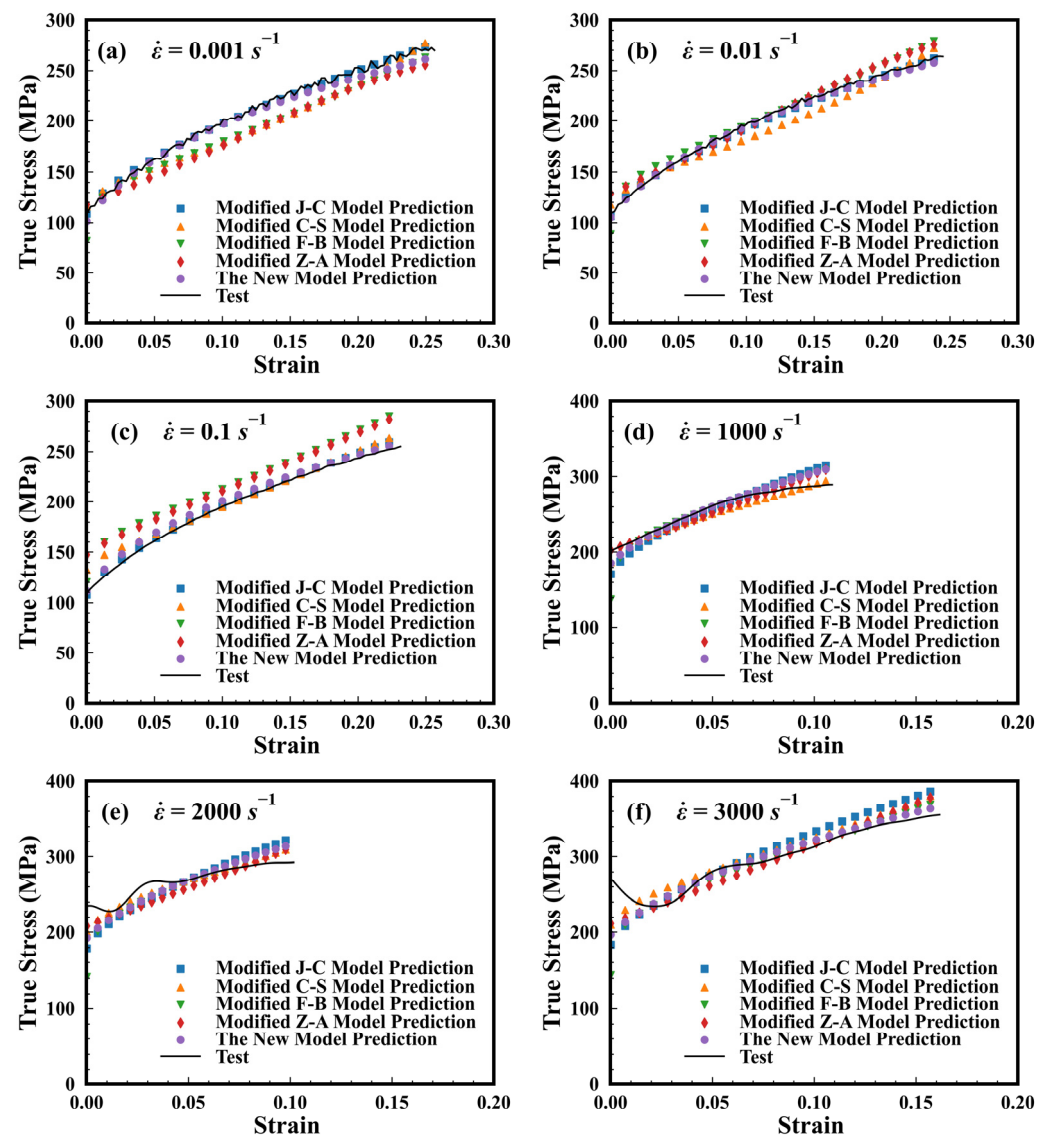


Figure 13. Comparison of the experimental results with the predicted stress of AA5052-O at different strain rates (a) 0.001 s^{-1} ; (b) 0.01 s^{-1} ; (c) 0.1 s^{-1} ; (d) 1000 s^{-1} ; (e) 2000 s^{-1} ; and (f) 3000 s^{-1} .

5. Conclusions

This paper compares the relationships of flow stress and strain at different strain rates ranging from 0.001 s^{-1} to 3000 s^{-1} and at different temperatures ranging from 293 K to 473 K to illustrate the influence of the dislocation evolution on the constitutive relationship over a wide strain-rate range. The experimental results show that the elongation of the material increases significantly under high-strain-rate conditions (up to 3000 s^{-1}). Moreover, a new physically-based constitutive model is proposed for the constitutive relationship of AA5052-O based on the Arrhenius model. The conclusions can be drawn as follows.

- (1) A new physically-based constitutive model is proposed, which considers the dynamic strain aging, the drag stress, and the evolution of mobile dislocation and forest dislocation, as well as the thermal activation mechanism. The flow stress under different temperature and strain-rate conditions predicted by the newly proposed constitutive model were close to the experimental data, and the model showed a high correlation coefficient of 0.99.
- (2) The yield stress predicted by the new constitutive model based on a modified Arrhenius model shows that the competition between dynamic strain aging and thermal

activation mechanisms is significant within the strain rate range of $0.001\text{--}1\text{ s}^{-1}$, and the thermal activation mechanism dominates in the range of $1\text{--}10^4$.

- (3) The evolution of mobile dislocation and forest dislocation is well depicted by the new constitutive model over a wide strain-rate range, and the relative error among model prediction results of dislocation density, TEM statistical results, and XRD data calculation results is at a low level.
- (4) The newly proposed model is compared with the modified J–C model, the modified C–S model, the modified F–B model, and the modified Z–A model, and the result shows that both the AARE and RMSE of the new model are the lowest, indicating a higher prediction accuracy.

Finally, it is worth noting that the new model is not only applicable to AA5052-O but also to aluminum alloys with or without the DSA effect that have dislocation strengthening as the primary source of strain hardening, especially for the Al–Mg aluminum alloy.

Author Contributions: Conceptualization, H.M. and P.W.; methodology, H.M. and P.W.; software, P.W.; validation, W.M. and H.Z.; formal analysis, H.M., P.W., W.M. and Z.G.; investigation, H.M. and X.H.; resources, H.M.; data curation, H.M. and X.H.; writing—original draft preparation, H.M., P.W. and Z.G.; writing—review and editing, M.Z. and H.Z.; visualization, P.W. and M.Z.; supervision, H.Z.; project administration, H.M.; funding acquisition, H.M. All authors have read and agreed to the published version of the manuscript.

Funding: This work was funded by the Knowledge Innovation Program of Wuhan-Shuguang Project, the National Natural Science Foundation of China (Grant Nos. 51905395, 52273319), the National Innovation and Entrepreneurship Training Program for College Students (202210497073), the Natural Science Foundation of Hubei Province (Grant No. 2020CFB550), the 111 Project (B17034), and the Innovative Research Team Development Program of Ministry of Education of China (IRT_17R83).

Data Availability Statement: The data presented in this study are available on request from the corresponding author. The data are not publicly available due to privacy.

Conflicts of Interest: The authors declare no conflict of interest.

References

1. Golovashchenko, S.F. Material Formability and Coil Design in Electromagnetic Forming. *J. Mater. Eng. Perform.* **2007**, *16*, 314–320. [\[CrossRef\]](#)
2. Lim, M.; Byun, H.; Song, Y.; Park, J.; Kim, J. Numerical Investigation on Comparison of Electromagnetic Forming and Drawing for Electromagnetic Forming Characterization. *Metals* **2022**, *12*, 1248. [\[CrossRef\]](#)
3. Tartière, J.; Arrigoni, M.; Nème, A.; Groeneveld, H.; Van Der Veen, S. PVDF Based Pressure Sensor for the Characterisation of the Mechanical Loading during High Explosive Hydro Forming of Metal Plates. *Sensors* **2021**, *21*, 4429. [\[CrossRef\]](#) [\[PubMed\]](#)
4. Babalo, V.; Mirzahosein, M.; Fazli, A.; Soltanpour, M. High-speed joining of tubes to panel sheets using electro-hydraulic forming. *Int. J. Adv. Manuf. Technol.* **2022**, *119*, 4713–4731. [\[CrossRef\]](#)
5. Tian, Y.; Huang, L.; Ma, H.; Li, J. Establishment and comparison of four constitutive models of 5A02 aluminium alloy in high-velocity forming process. *Mater. Des.* **2014**, *54*, 587–597. [\[CrossRef\]](#)
6. Thomas, J.D.; Seth, M.; Daehn, G.S.; Bradley, J.R.; Triantafyllidis, N. Forming limits for electromagnetically expanded aluminum alloy tubes: Theory and experiment. *Acta Mater.* **2007**, *55*, 2863–2873. [\[CrossRef\]](#)
7. Balanethiram, V.S.; Daehn, G.S. Enhanced formability of interstitial free iron at high strain rates. *Scr. Mater.* **1992**, *27*, 1783–1788. [\[CrossRef\]](#)
8. Wu, J.; Djavanroodi, F.; Gode, C.; Ebrahimi, M.; Attarilar, S. Microstructure evolution, texture development, and mechanical properties of hot-rolled 5052 aluminum alloy followed by annealing. *Mater. Res. Express* **2022**, *9*, 056516. [\[CrossRef\]](#)
9. Wu, J.; Djavanroodi, F.; Shamsborhan, M.; Attarilar, S.; Ebrahimi, M. Improving Mechanical and Corrosion Behavior of 5052 Aluminum Alloy Processed by Cyclic Extrusion Compression. *Metals* **2022**, *12*, 1288. [\[CrossRef\]](#)
10. Idriss, M.; Mirakhorli, F.; Desrochers, A.; Maslouhi, A. Overlap laser welding of 5052-H36 aluminum alloy: Experimental investigation of process parameters and mechanical designs. *Int. J. Adv. Manuf. Technol.* **2022**, *119*, 7653–7667. [\[CrossRef\]](#)
11. Chen, F.; Qu, H.; Wu, W.; Zheng, J.-H.; Qu, S.; Han, Y.; Zheng, K. A Physical-Based Plane Stress Constitutive Model for High Strength AA7075 under Hot Forming Conditions. *Metals* **2021**, *11*, 314. [\[CrossRef\]](#)
12. dos Santos, T.; Rossi, R.; Maghous, S.; Rosa, P.A.R. Mechanical characterization and constitutive modeling of aluminum AA1050 subjected to high strain-rates. *Mech. Time-Depend. Mater.* **2021**, *26*, 347–375. [\[CrossRef\]](#)
13. Fan, Z.; Song, Z.; Xiao, D.; Ribárik, G.; Ungár, T. Influence of Deformation Temperature On Flow Stress and Dislocation Structure of 2A12 Aluminum Alloy Under Quasi-Static and Dynamic Compression. *Exp. Mech.* **2023**, *63*, 703–714. [\[CrossRef\]](#)

14. Dong, F.; Yi, Y.; Huang, S.; Gao, S.; Jia, Y.; Yu, W. A dislocation density-based model considering dynamic strain aging for annealed and water-quenched aluminum alloys under low-temperature conditions. *Mater. Sci. Eng. A* **2022**, *855*, 143916. [[CrossRef](#)]
15. Wang, Y.; Peng, J.; Zhong, L.; Pan, F. Modeling and application of constitutive model considering the compensation of strain during hot deformation. *J. Alloys Compd.* **2016**, *681*, 455–470. [[CrossRef](#)]
16. Xia, Y.; Jiang, W.; Cheng, Q.; Jiang, L.; Jin, L. Hot deformation behavior of Ti—6Al—4V—0.1Ru alloy during isothermal compression. *Trans. Nonferrous Met. Soc. China* **2020**, *30*, 134–146. [[CrossRef](#)]
17. Xue, D.; Wei, W.; Shi, W.; Zhou, X.; Rong, L.; Wen, S.; Wu, X.; Qi, P.; Gao, K.; Huang, H.; et al. Microstructural evolution and constitutive analysis of Al-Mg-Zn-Er-Zr based on arrhenius-type and machine-learning algorithm. *Mater. Today Commun.* **2022**, *32*, 104076. [[CrossRef](#)]
18. Zhang, Y.; Jiang, J.; Wang, Y.; Liu, Y.; Huang, M. Hot deformation behavior and microstructure evolution of hot-extruded 6A02 aluminum alloy. *Mater. Charact.* **2022**, *188*, 111908. [[CrossRef](#)]
19. Zhang, Y.; Yang, L.; Fan, Z.; Pang, S.; Chen, W. Evaluation of tensile creep behavior of spray formed and extruded 7075 aluminum alloy by equivalent stress. *J. Mater. Res. Technol.* **2023**, *22*, 1476–1490. [[CrossRef](#)]
20. Li, H.; Li, X.; Yan, H.; Li, Y.; Geng, L.; Xun, C.; Li, Z.; Zhang, Y.; Xiong, B. Constitutive Analysis and Microstructure Characteristics of As-Homogenized 2198 Al-Li Alloy under Different Hot Compression Deformation Conditions. *Materials* **2023**, *16*, 2660. [[CrossRef](#)]
21. GB/T 3880.2 2012; Wrought Aluminium and Aluminium Alloy Plates, Sheets and Strips for General Engineering Part 2: Mechanical Properties. Standards Press of China: Beijing, China, 2012. (In Chinese)
22. ISO 6892-1:2019; Metallic Materials—Tensile Testing—Part 1: Method of Test at Room Temperature. ISO: Geneva, Switzerland, 2019.
23. Khan, A.S.; Liang, R. Behaviors of three BCC metal over a wide range of strain rates and temperatures: Experiments and modeling. *Int. J. Plast.* **1999**, *10*, 1089–1109. [[CrossRef](#)]
24. Muiruri, A.; Maringa, M.; du Preez, W. Numerical Simulation of High Strain Rate and Temperature Properties of Laser Powder Bed Fusion Ti6Al4V(ELI) Determined Using a Split Hopkinson Pressure Bar. *Materials* **2022**, *15*, 1872. [[CrossRef](#)] [[PubMed](#)]
25. Weber, L.; Kouzeli, M.; Marchi, C.S.; Mortensen, A. On the use of Considere's criterion in tensile testing of materials which accumulate internal damage. *Scr. Mater.* **1999**, *41*, 549–551. [[CrossRef](#)]
26. Zhu, Y.; Fan, J.; Li, Z.; Luo, Y.; Niu, Y. Study of strain rate sensitivity exponent and strain hardening exponent of typical titanium alloys. *Mater. Today Commun.* **2022**, *30*, 103060. [[CrossRef](#)]
27. Fang, J.; Zhu, Z.; Zhang, X.; Xie, L.; Huang, Z. Tensile Deformation and Fracture Behavior of AA5052 Aluminum Alloy under Different Strain Rates. *J. Mater. Eng. Perform.* **2021**, *30*, 9403–9411. [[CrossRef](#)]
28. Mesbah, M.; Faraji, G.; Bushroa, A.R. Electron back-scattered diffraction and nanoindentation analysis of nanostructured Al tubes processed by multipass tubular-channel angular pressing. *Met. Mater. Int.* **2016**, *22*, 288–294. [[CrossRef](#)]
29. Li, N.; Yu, H.; Xu, Z.; Fan, Z.; Liu, L. Electromagnetic forming facilitates the transition of deformation mechanism in 5052 aluminum alloy. *Mater. Sci. Eng. A* **2016**, *673*, 222–232. [[CrossRef](#)]
30. Monteiro, S.N.; Brandão, L.P.; de Sousa, T.G.; Filho, F.d.C.G. Novel methods for dislocation density estimation in highly compacted tangles. *J. Mater.* **2019**, *9*, 2072–2078. [[CrossRef](#)]
31. Ham, R.K. The determination of dislocation densities in thin films. *Philos. Mag.* **1961**, *6*, 1183–1184. [[CrossRef](#)]
32. Liang, Z.; Li, Y.; Huang, M. The respective hardening contributions of dislocations and twins to the flow stress of a twinning-induced plasticity steel. *Scr. Mater.* **2016**, *112*, 28–31. [[CrossRef](#)]
33. Guo, N.; Liu, T.; Luan, B.; Wang, B.; Liu, Q. Dislocation density and configuration in fully pearlitic steel during wire drawing. *Mater. Res. Innov.* **2014**, *18*, S4–249. [[CrossRef](#)]
34. Suo, T.; Chen, Y.; Li, Y.; Wang, C.; Fan, X. Strain rate sensitivity and deformation kinetics of ECAPed aluminium over a wide range of strain rates. *Mater. Sci. Eng. A* **2013**, *560*, 545–551. [[CrossRef](#)]
35. Lee, W.-S.; Chen, T.-H.; Lin, C.-F.; Chen, M.S. Impact deformation behaviour and dislocation substructure of Al-Sc alloy. *J. Alloys Compd.* **2010**, *493*, 580–589. [[CrossRef](#)]
36. Carvalho-Silva, V.H.; Coutinho, N.D.; Aquilanti, V.; Simos, T.E.; Kalogiratos, Z.; Monovasilis, T. Description of deviations from Arrhenius behavior in chemical kinetics and materials science. *AIP Conf. Proc.* **2016**, *1790*, 4968632. [[CrossRef](#)]
37. Eivani, A.; Vafaeezad, H.; Nikan, O.; Zhou, J. Modeling high temperature deformation characteristics of AA7020 aluminum alloy using substructure-based constitutive equations and mesh-free approximation method. *Mech. Mater.* **2019**, *129*, 104–112. [[CrossRef](#)]
38. Orowan, E. Problems of plastic gliding. *Proc. Phys. Soc.* **1940**, *52*, 8–22. [[CrossRef](#)]
39. Zerilli, F.; Armstrong, R. The effect of dislocation drag on the stress-strain behavior of F.C.C. metals. *Acta Mater.* **1992**, *40*, 1803–1808. [[CrossRef](#)]
40. Huang, C.-Q.; Deng, J.; Wang, S.-X.; Liu, L.-L. A physical-based constitutive model to describe the strain-hardening and dynamic recovery behaviors of 5754 aluminum alloy. *Mater. Sci. Eng. A* **2017**, *699*, 106–113. [[CrossRef](#)]
41. Zaretsky, E.B.; Kanel, G.I. Effect of temperature, strain, and strain rate on the flow stress of aluminum under shock-wave compression. *J. Appl. Phys.* **2012**, *112*, 73504. [[CrossRef](#)]
42. Jiang, H.; Zhang, Q.; Chen, X.; Chen, Z.; Jiang, Z.; Wu, X.; Fan, J. Three types of Portevin–Le Chatelier effects: Experiment and modelling. *Acta Mater.* **2007**, *55*, 2219–2228. [[CrossRef](#)]

43. Lin, Y.; Yang, H.; He, D.-G.; Chen, J. A physically-based model considering dislocation–solute atom dynamic interactions for a nickel-based superalloy at intermediate temperatures. *Mater. Des.* **2019**, *183*, 108122. [[CrossRef](#)]
44. Wang, J.; Guo, W.-G.; Gao, X.; Su, J. The third-type of strain aging and the constitutive modeling of a Q235B steel over a wide range of temperatures and strain rates. *Int. J. Plast.* **2015**, *65*, 85–107. [[CrossRef](#)]
45. Kubin, L.; Estrin, Y. Evolution of dislocation densities and the critical conditions for the Portevin-Le Châtelier effect. *Acta Mater.* **1990**, *38*, 697–708. [[CrossRef](#)]
46. Csanádi, T.; Chinh, N.Q.; Gubicza, J.; Langdon, T.G. Plastic behavior of fcc metals over a wide range of strain: Macroscopic and microscopic descriptions and their relationship. *Acta Mater.* **2011**, *59*, 2385–2391. [[CrossRef](#)]
47. Qiu, M.; Cao, P.; Cao, L.; Tan, Z.; Hou, C.; Wang, L.; Wang, J. Parameter Determination of the 2S2P1D Model and Havriliak–Negami Model Based on the Genetic Algorithm and Levenberg–Marquardt Optimization Algorithm. *Polymers* **2023**, *15*, 2540. [[CrossRef](#)] [[PubMed](#)]
48. Nieto-Fuentes, J.; Rittel, D.; Osovski, S. On a dislocation-based constitutive model and dynamic thermomechanical considerations. *Int. J. Plast.* **2018**, *108*, 55–69. [[CrossRef](#)]
49. Song, P.; Li, W.; Wang, X.; Xu, W. Study on mechanical properties and constitutive model of 5052 aluminium alloy. *Mater. Sci. Technol.* **2019**, *35*, 916–924. [[CrossRef](#)]
50. Geng, P.; Qin, G.; Zhou, J.; Zou, Z. Hot deformation behavior and constitutive model of GH4169 superalloy for linear friction welding process. *J. Manuf. Process.* **2018**, *32*, 469–481. [[CrossRef](#)]
51. Samantaray, D.; Mandal, S.; Bhaduri, A. Constitutive analysis to predict high-temperature flow stress in modified 9Cr–1Mo (P91) steel. *Mater. Des.* **2010**, *31*, 981–984. [[CrossRef](#)]
52. Sabokpa, O.; Zarei-Hanzaki, A.; Abedi, H.; Haghdadi, N. Artificial neural network modeling to predict the high temperature flow behavior of an AZ81 magnesium alloy. *Mater. Des.* **2012**, *39*, 390–396. [[CrossRef](#)]

Disclaimer/Publisher’s Note: The statements, opinions and data contained in all publications are solely those of the individual author(s) and contributor(s) and not of MDPI and/or the editor(s). MDPI and/or the editor(s) disclaim responsibility for any injury to people or property resulting from any ideas, methods, instructions or products referred to in the content.